



OPEN

## [<sup>18</sup>F]-Labeled PARP-1 PET imaging of PSMA targeted alpha particle radiotherapy response

Hanwen Zhang<sup>1,2,12</sup>, Diane Abou<sup>1,2,3</sup>, Peng Lu<sup>1,2,11</sup>, Abbie Meghan Hasson<sup>1,2,11</sup>, Alexandria Villmer<sup>1,2</sup>, Nadia Benabdallah<sup>1,2</sup>, Wen Jiang<sup>2,4</sup>, David Ulmert<sup>5,6</sup>, Sean Carlin<sup>7</sup>, Buck E. Rogers<sup>2,8</sup>, Norman F. Turtle<sup>1</sup>, Michael R. McDevitt<sup>9</sup>, Brian Baumann<sup>2,8</sup>, Brian W. Simons<sup>10</sup>, Farrokh Dehdashti<sup>1,12</sup>, Dong Zhou<sup>1✉</sup> & Daniel L. J. Thorek<sup>1,2,11,12✉</sup>

The growing interest and clinical translation of alpha particle ( $\alpha$ ) therapies brings with it new challenges to assess target cell engagement and to monitor therapeutic effect. Noninvasive imaging has great potential to guide  $\alpha$ -treatment and to harness the potential of these agents in the complex environment of disseminated disease. Poly(ADP) ribose polymerase 1 (PARP-1) is among the most abundantly expressed DNA repair enzymes with key roles in multiple repair pathways—such as those induced by irradiation. Here, we used a third-generation PARP1-specific radiotracer, [<sup>18</sup>F]-PARPZ, to delineate castrate resistant prostate cancer xenografts. Following treatment with the clinically applied [<sup>225</sup>Ac]-PSMA-617, positron emission tomography was performed and correlative autoradiography and histology acquired. [<sup>18</sup>F]-PARPZ was able to distinguish treated from control (saline) xenografts by increased uptake. Kinetic analysis of tracer accumulation also suggests that the localization of the agent to sites of increased PARP-1 expression is a consequence of DNA damage response. Together, these data support expanded investigation of [<sup>18</sup>F]-PARPZ to facilitate clinical translation in the  $\alpha$ -therapy space.

Radiation is a mainstay of cancer therapy, most often generated by linear accelerator systems with image guidance<sup>1</sup>. Indeed, approximately 50% of all cancer patients will receive radiation of some form during their treatment. In the metastatic setting, radiation delivery becomes much more complex as planning for treatment at multiple foci must also ensure that neighboring healthy tissues do not receive ablative doses. Thus, radiation to treat disseminated disease is less frequently applied. The use of targeted radiation delivery from beta or alpha particles that are administered systemically and localize to deposits of disease overcomes several of these issues<sup>2</sup>.

Alpha particles ( $\alpha$ ) are of particular interest as these high-energy, high linear energy transfer helium nuclei deliver tumoricidal doses with emissions that are highly localized<sup>3</sup>. Recently, Radium-223 dichloride, the first approved drug in this class, was marketed for the management of bone metastases in castrate resistant prostate cancer patients<sup>4</sup>. This follows a successful Phase III clinical trial which demonstrated an overall survival advantage for patients receiving the bone-targeted agent<sup>5</sup>. The approval of Radium-223 and the initial clinical investigation of other targeted alpha particle ( $\alpha$ )-therapy vehicles<sup>6–9</sup>, has led to an increased interest in the utilization of these potent emitters. An isotope of considerable interest for these applications is the actinide Actinium-225 which produces four  $\alpha$ 's through it and its daughters' decay. Preclinical and clinical evaluation of this isotope, conjugated to antibodies and small molecules, is ongoing<sup>10–13</sup>.

<sup>1</sup>Department of Radiology, Washington University School of Medicine, 510 S. Kingshighway Blvd., Campus, Box 8225, St. Louis, MO 63110, USA. <sup>2</sup>Program in Quantitative Molecular Therapeutics, Washington University School of Medicine, St. Louis, MO, USA. <sup>3</sup>Radiology Cyclotron Facility, Mallinckrodt Institute of Radiology, Washington University in St. Louis, St. Louis, MO, USA. <sup>4</sup>Department of Biomedical Engineering, Johns Hopkins University, Baltimore, MD, USA. <sup>5</sup>Johnsson Comprehensive Cancer Center, University of California, Los Angeles, CA, USA. <sup>6</sup>Department of Molecular and Medical Pharmacology, University of California Los Angeles, Los Angeles, CA, USA. <sup>7</sup>Department of Radiology, University of Pennsylvania, Philadelphia, PA, USA. <sup>8</sup>Department of Radiation Oncology, Washington University School of Medicine, St. Louis, MO, USA. <sup>9</sup>Department of Radiology, Memorial Sloan Kettering Cancer Center, New York, NY, USA. <sup>10</sup>Center for Comparative Medicine, Baylor College of Medicine, Houston, TX, USA. <sup>11</sup>Department of Biomedical Engineering, Washington University in St. Louis, St. Louis, MO, USA. <sup>12</sup>Oncologic Imaging Program, Siteman Cancer Center, Washington University School of Medicine, St. Louis, MO, USA. ✉email: zhoud@wustl.edu; thorek.lab@wustl.edu

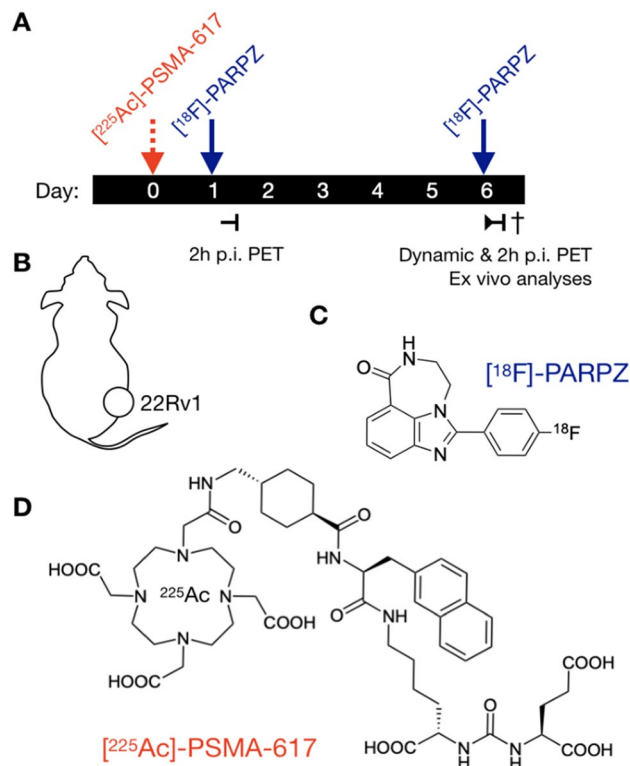


**Figure 1.** Schematic of Study Design. A) PSMA-expressing 22Rv1-Luc subcutaneous xenograft were implanted into NCI athymic Nu/Nu male. Upon reaching approximately 500 mm<sup>3</sup>, either control saline or the potent targeted [<sup>225</sup>Ac]-PSMA-617 was administered. Static [<sup>18</sup>F]PARPZ-PET was performed at 1 and 6 d post-therapy (n = 8), and dynamic imaging for group matched animals (n = 3). Chemical structures of A) the PARP-1 specific [<sup>18</sup>F]-PARPZ radiotracer and B) the prostate cancer targeting [<sup>225</sup>Ac]-PSMA-617.

The double strand DNA breaks and severe genotoxic damage incurred by  $\alpha$ -traversal of the nucleus are difficult to repair. In controlled in vitro study, a single  $\alpha$  can kill a target cell<sup>14</sup>. However, the short path length of these emission means that many cells are spared any exposure; as evinced in part by the fact that these are not curative treatments<sup>5,15</sup>. Furthermore, we have shown previously that genomic factors such as DNA damage repair (DDR) status may influence sensitivity to  $\alpha$ -therapy<sup>16</sup>. We and others posit that detection of DDR, ideally through non-invasive methods, can be used to personalize treatment approaches<sup>17–20</sup>.

The multipathway mechanisms of eukaryotic DDR are intricate, orchestrated and tightly controlled processes. Summarily, these involve sensing of damage, signal transduction and recruitment of enzymatic complexes to remodel and repair DNA. Poly (ADP-ribose) polymerase 1 (PARP-1) is among the most well studied DDR proteins<sup>21–23</sup> and has critical roles in multiple single and double strand repair processes<sup>24</sup>. As such, inhibition of catalytic activity of this enzyme, and in particular the PARP-1 isoform, has been exploited to induce synthetic lethality in combination with loss of BRCA1 or BRCA2 function. The capacity to assess the PARP-1 status in a target cancer cell is emerging as a means to select patients for and to monitor PARP-1 inhibitor therapy<sup>25,26</sup>.

[<sup>18</sup>F]PARPZ, also known as [<sup>18</sup>F]WC-DZ-F, was developed as an analogue of [<sup>18</sup>F]FluorThanatrace (FTT) and [<sup>125</sup>I] KX1 which are well-established PARP-1 ligands for measuring PARP-1 expression. Our previous work has shown that this third-generation radiolabeled PARP-1 inhibitor has highly specific targeted uptake and favorable pharmacokinetic properties for use as a non-invasive imaging agent and targeted therapy<sup>27</sup>. We aimed here to determine if [<sup>18</sup>F]PARPZ can be used to report changes in PARP-1 expression following targeted  $\alpha$ -therapy. We have used the 22Rv1 model of prostate cancer, and treated xenograft-bearing mice with [<sup>225</sup>Ac]-PSMA-617 (Fig. 1). The 22Rv1 cell line is a BRCA-1 null, PARP-1 and prostate specific membrane antigen (PSMA)-expressing cell line that recapitulates the disease phenotype displayed by men in the castrate resistant setting. A comparison of common prostate and prostate cancer PARP-1 and PSMA expression is presented in Fig. 2. PSMA-617 is a chelate-conjugated peptide that targets prostate specific membrane antigen (PSMA, also known as Glutamate carboxypeptidase II [GCPII] and Folate Hydrolase 1 [FOLH1]), a cell surface receptor of considerable clinical and research interest in prostate cancer<sup>6,28,29</sup>, recently approved by the FDA for use with the beta particle emitting isotope <sup>177</sup>Lu. Here we evaluate uptake prior to and in response to therapy by [<sup>18</sup>F]PARPZ-PET.

## Materials and methods

**Synthesis and radiosynthesis of [<sup>18</sup>F]PARPZ.** [<sup>18</sup>F]PARPZ was synthesized and prepared for injection as previously described<sup>27</sup>, with improvements. [<sup>18</sup>F]-PARPZ was synthesized by two steps according to previously reported procedure. Synthesis of 4-[<sup>18</sup>F]fluorobenzaldehyde ([<sup>18</sup>F]2): Into a 10 mL Pyrex tube contain-

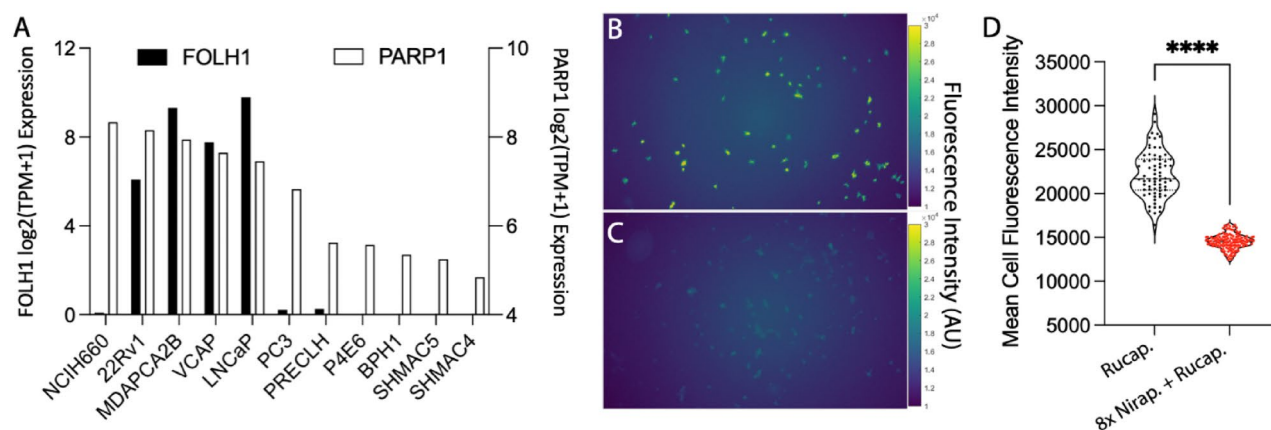


**Figure 2.** Cell Model Selection. (A) Evaluation of expression of *FOLH1* and *PARP1* in prostate and prostate cancer cell lines. (B) Fluorescence of rucaparib binding and uptake in 22Rv1 cells, (C) or blocked with excess non-fluorescent competitor niraparib. (D) Quantitation of mean fluorescence cell intensity following single cell segmentation ( $n > 70$ ).

ing 4-formyl-*N,N,N*-trimethylbenzenaminium triflate precursor (3.2 mg, 10.2  $\mu$ mol) and  $K_2CO_3/K_{222}$  (2.8 mg, 3.1  $\mu$ mol) was added [ $^{18}F$ ]tosyl fluoride (1.32 GBq) in acetonitrile (0.5 mL). The reaction mixture was shaken and then heated in an oil bath at 108 °C for 7 min. Synthesis of [ $^{18}F$ ]-PARPZ: At room temperature, the above reaction mixture passed through a Waters MCX cartridge (100 mg in 1 mL cartridge, pretreated with 3 mL acetonitrile), following by acetonitrile (0.5 mL) for rinsing, and all were eluted into a 10 mL Pyrex tube containing precursor 1 (2.6 mg, 14.7  $\mu$ mol) and 10% Pd/C (6 mg) in methanol (0.5 mL). The tube was flushed with argon, and then capped firmly and heated at 120 °C in a heating block. After 20 min, the reaction was completed according to HPLC. The reaction mixture passed through a pad of Celite (pre-treated with acetonitrile), and the reaction tube and Celite were rinsed with acetonitrile (2 mL). All the eluted solution was collected in a tube, and solvents were removed under a flow of argon at 108 °C. The residue was dissolved in HPLC mobile phase/water 1:1 (4 mL), and injected onto HPLC via a nylon filter. After HPLC purification (Agilent SB-C18 250  $\times$  9.4 mm, 17% acetonitrile/83% water/0.1% TFA, 4 mL/min, 250 nm), [ $^{18}F$ ]-PARPZ (0.44 GBq) was collected at 11 min and diluted in water (40 mL). [ $^{18}F$ ]-PARPZ was extracted from the solution by a standard solid phase extract procedure using a Waters HLB light and was formulated in 10% ethanol/saline.

**Radiolabeling of [ $^{225}Ac$ ]-PSMA-617.** Actinium-225 was supplied as a dry nitrate (Oak Ridge National Laboratory, Department of Energy). [ $^{225}Ac$ ]-PSMA-617 was prepared by dissolving 10  $\mu$ g peptide in 97.5  $\mu$ L 0.25 M HEPES buffer (pH 8.6), and adding 185 KBq [ $^{225}Ac$ ]( $NO_3$ )<sub>3</sub> solution (2.5  $\mu$ L) followed by a 15 min incubation at 97 °C. After incubation, the reaction solution was analyzed with TLC (C18; AcCN/10 mM EDTA buffer (1/9) as mobile), and the labeling yield was greater than 95%. After purification with Strata-X PRO cartridge (Phenomenex), the final product was eluted with 150  $\mu$ L ethanol and reformulated with PBS/BSA (1.0% bovine serum albumin) solution for injection (11 KBq [ $^{225}Ac$ ]-PSMA-617 in 100  $\mu$ L per mouse).

**Cells and fluorescence microscopy.** Evaluation of expression levels of genes of interest was accessed from the Broad Institute Cancer Cell Line Encyclopedia<sup>30,31</sup>. The selected cell line for the current study is 22Rv1 (a gift of Dr. Kenneth James Pienta of Johns Hopkins University), which 200,000 cells are seeded in 12-well plate at the day before experiments. After 1 h incubation with Rucaparib (25  $\mu$ M) with or without Niraparib (200  $\mu$ M) at 37 °C, and medium removal and wash with 2  $\times$  1.0 mL of PBS, the cells were scanned using a 10  $\times$  Fluor Plan Apo objective (Nikon) and exposure time of 1 s with a DAPI filter, using an automated inverted fluorescence microscope (Nikon Eclipse Ti2). Acquisition parameters were controlled using NIS-Elements (Nikon, version Ar). After scanning, Ilastik (version 1.3.2post1) was used to generate single cell masks. The segmented cell masks along with the raw images were used to calculate the single cell expressions with customized Matlab scripts (R2021a, MathWorks). The cell expressions were compared with non-paired Student's T test in Prism 9 (Graph-Pad Software Inc.).

**Animal studies.** All animal studies were performed under the Guide for the Care and Use of Laboratory Animals through the Washington University Animal Studies Committee, which conform to ARRIVE guidelines (<https://arriveguidelines.org>) protocol #2019006. The tumor model used for these studies were 22Rv1-Luc cells grown in conditions specified by the American Type Culture Collection. Four million cells were implanted in a 1:1 mixture of cells in DPBS (ThermoFisher) and matrigel (Corning) into NCI Athymic NCR-nu/nu male mice (8wk; Charles River/NCI). Tumors were monitored by bioluminescence and caliper measurements, and used for treatment and imaging upon reaching approximately 500 mm<sup>3</sup>. A larger tumor volume than for traditional tumor control studies was chosen for the present investigations to preclude full local tumor control in the therapy group; reducing the variability of tumor size between groups.

Tumor bearing mice were anesthetized with isoflurane (2% mixture in 2 L/min) and radioligand were delivered by injection into the retro-orbital sinus<sup>32</sup>. 11.1 KBq of [<sup>225</sup>Ac]-PSMA-617 was administered to each of the animals in the treatment group. For dynamic imaging, an animal from each treatment and control group were simultaneously injected with approximately 7.4 MBq on the bed of the dedicated small animal tomograph (microPET R4, Concorde Microsystems), in triplicate, and imaged for 30 min. All static images were acquired for 10 min at between 110 and 130 min post-administration. Acquisitions were recorded using an energy window of 350–700 keV and coincidence-timing window of 6 ns. PET image data were corrected for detector non-uniformity, deadtime, random coincidences and physical decay. The instrument was calibrated using a <sup>18</sup>F-filled quantitation phantom. The 30 min duration datasets were histogrammed to 5 min frames and were reconstructed using a *maximum* a priori MAP and 3D filtered back projection using a ramp filter with a cut-off frequency equal to the Nyquist frequency into a 128 × 128 × 63 matrix. Region of interest analysis was conducted in ASIPro (v6.3.3.0, Concorde Microsystems) and statistical analyses were performed in Prism (v8.0, GraphPad Software).

**Autoradiography and Immunohistochemistry.** Fresh frozen sections of [<sup>225</sup>Ac]-PSMA-617 treated tumors were prepared and exposed, as previously<sup>33,34</sup>. Briefly, 8 μm thick sections in O.C.T. Compound (TissuePlus, Fisher Healthcare) were fixed opposite a storage phosphor screen (MS, PerkinElmer) at –20 °C for 3 days. Imaging and analysis were performed on the CyclonePlus and Optiquant (v4.1, PerkinElmer). Contrast limited enhanced histogram equalization was performed on the lossless image and displayed with an optimized colormap (Viridis<sup>35</sup>) using FIJI<sup>36</sup>.

Sectioned tissue slides were fixed briefly in 4% paraformaldehyde (Affymetrix), dried and stored. Slides were rehydrated before steaming in EDTA pH 8 (Invitrogen) for 40 min. Endogenous peroxidases were quenched with BLOXALL (Vector Labs), and the slides were blocked for 1 h with Serum Free Protein Block (Dako). Slides were incubated with antibodies directed against PARP-1 (Abcam ab194586). Staining was visualized with ImmPRESS Polymer detection kit and ImmPACT DAB (Vector Labs).

## Results

**Cell model.** In order to test the capability of PSMA-targeted alpha particle therapy in a clinically relevant preclinical setting, we evaluated cell lines for both PARP1 and PSMA expression. We compared the expression *PARP1* and *FOLH1* across a range of prostate and prostate cancer cells Fig. 2A. 22Rv1 expresses both targets; and we then evaluated the specificity of uptake of rucaparib in these cells by fluorescence microscopy. PARPZ is derivatized from the rucaparib scaffold, containing the nicotinamide pharmacophore (Fig. 1C), and 22Rv1 cells fluorescence increased under UV excitation after incubation with the drug<sup>37,38</sup>. The PARP specificity of this interaction was confirmed by blocking with an excess of niraparib, a PARP1/2 inhibitor with similar affinity<sup>39</sup>, and was quantitated on a single cell basis (Fig. 2B–D).

**Radiochemistry.** [<sup>18</sup>F]-PARPZ was synthesized from a 4-fluorobenzaldehyde precursor using an improved procedure for greater yield<sup>27</sup>. We achieved a radiochemical yield of 52% and radiochemical purity of 99.9% at the end of synthesis. Specific activity of the tracer at preparation was 76 GBq/μmol per synthesis. Baseline PARP-1 imaging was performed at 2 h post administration of [<sup>18</sup>F]-PARPZ on day one of the imaging study (Fig. 1). We chose the 6 day treatment date for follow-up imaging as we would not expect significant differences between saline control and [<sup>225</sup>Ac]-PSMA-617 treated 22Rv1 tumors at this interim time. The half-life of Actinium-225 is 10 days, and the energy deposited from the initially localized radiotherapy at day 6 will be roughly 35% of the total dose. Indeed tumor volumes between the groups were not significantly different at either imaging dates.

**[<sup>18</sup>F]-PARPZ PET.** We performed PET imaging of treated and control groups at day 1 and day 6 post-administration. Figure 3 shows coronal slices (left) and maximum intensity projection (right) images for representative control untreated (top) and [<sup>225</sup>Ac]-PSMA-617 treated (bottom) animals from the two imaging time points. As expected, hepatobiliary clearance resulted in a majority of PARP tracer activity in the intestine at the imaging timepoints indicated in both baseline and treatment PET acquisitions. Distinction of the tumor can be made in all subjects using [<sup>18</sup>F]-PARPZ (as annotated with an arrow, Fig. 3A–D). Qualitatively, there are no notable differences in tracer distribution or tumor delineation between the control and treated subjects at day 1 or the untreated animals at day 6. Prominent uptake in the treated tumor in the latter (day 6) imaging session (Fig. 3D) is observed, and more clearly resolved in the projection imaging data (Fig. 3H).

Quantitation of [<sup>18</sup>F]-PARPZ PET uptake in tumors was assessed noninvasively and compared across control and treatment groups between the two imaging timepoints (Fig. 4A,C). No significant difference in the tracer localization was noted between control and [<sup>225</sup>Ac]PSMA-617 groups at the initial baseline (1 day post-administration) scan. Likewise, no difference in mean or maximum tumor uptake was noted in the untreated group between day 1 and day 6 timepoints. In contrast, there was both a significant difference in PARP-1 tracer localization (mean percent injected activity per gram) for the treated group between the initial and latter scan dates ( $P < 0.01$ ); as well as a measurable difference between the control and treated tumor uptake at day 6 ( $P < 0.05$ ). Maximum tumor uptake as percent injected activity per gram was also significant between the treated animals across the two imaging timepoints ( $P = 0.05$ ).

The change in mean and maximum [<sup>18</sup>F]-PARPZ uptake on an individual subject basis is shown in Fig. 4B,D. The maximum intensity values increase in nearly all tumors investigated. We surmise that the increase in this metric is a function of both therapy induced DNA damage induced expression of PARP-1, as well as increased tumor cell PARP-1 expression in controls resulting from tumor progression.

A subset of animals were imaged on-camera upon tracer administration at the 6 day post-treatment imaging session in order to investigate the kinetics of tumor localization. The (mean) percent injected activity per gram

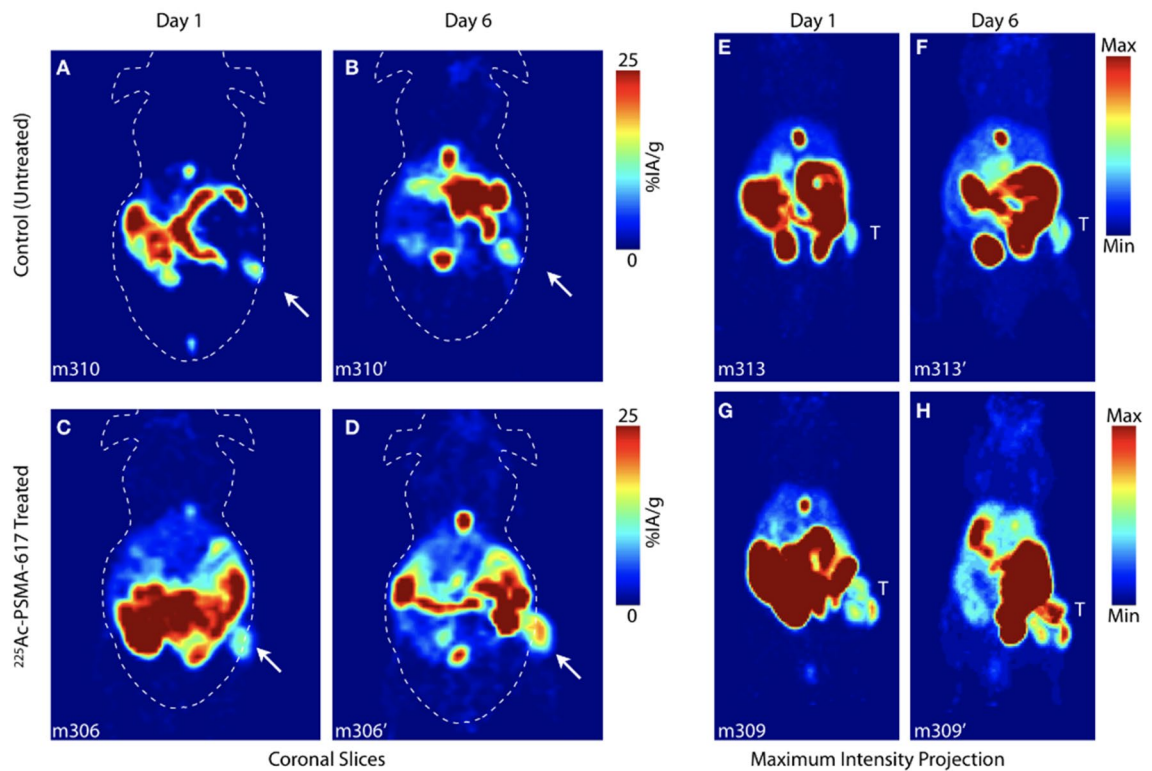


**Figure 3.** [ $^{18}\text{F}$ ]-PARPZ PET Imaging of Control and Alpha Particle Irradiated Tumors. Coronal slice of representative control mouse bearing 22Rv1-Luc xenografts at (A) Day 1 and (B) Day 6. Whole-body coronal PET slice of [ $^{225}\text{Ac}$ ]-PSMA-617 treated subject at (C) Day 1 and (D) Day 6. Distribution to the intestine (and gall bladder) recapitulates our previous work<sup>27</sup>; and tumor is delineated as indicated (arrow). Representative Day 1 and Day 6 whole body maximum intensity projection (MIP) data for control (top) and treated (bottom) groups; tumor denoted (T).

accumulation in the tumor was recorded across 180 s frames out to 30 min. Two representative animals from each saline control and treated groups were imaged together on the imaging bed, and are plotted in Fig. 5. These kinetic scans show more rapid uptake at an increased magnitude for the [ $^{225}\text{Ac}$ ]-PSMA-617 treated subjects.

**Autoradiography and immunohistochemistry.** The dissected tumor tissue were sectioned and evaluated for [ $^{225}\text{Ac}$ ]-PSMA-617 signal by autoradiography in the treatment group and both groups were immunostained for PARP-1 (Fig. 6). These tumors expressed PARP-1 either throughout, or in defined, non-stromal areas. As expected, the areas for which PARP-1 staining was present generally correlated with [ $^{225}\text{Ac}$ ]-PSMA-617 localization by phosphor autoradiography (Fig. 6A–D). No significant difference in staining intensity was observed between control and treated groups by immunohistochemistry. However, there was a trend towards more intense PARP-1 staining in the [ $^{225}\text{Ac}$ ]-PSMA-617 irradiated over the control saline-treated tumors. These qualitative results recapitulate the [ $^{18}\text{F}$ ]-PARPZ imaging results (Figs. 2, 3), with increases in the radioligand treatment group, along with baseline PARP-1 imaging in all 22Rv1 tumors.

## Discussion

We have evaluated the utility of a PARP-1 tracer to delineate responses to targeted alpha particle radiotherapy in a mouse model of prostate cancer. This work shows that we are able to quantitatively distinguish [ $^{18}\text{F}$ ]-PARPZ uptake in tumors treated with an  $\alpha$  emitting targeted radiotherapy,  $^{225}\text{Ac}$ -PSMA-617. The general focus of extant PARP-1 positron emitting radiotracer work has been to evaluate and validate PARP-1 expression for eventual clinical use<sup>25,26,40</sup>. This may provide the capacity to characterize PARP-1 expression in patients which may help to guide selection and dosing of PARP inhibitors, of which several are clinically approved for various indications<sup>41</sup>.

Previous investigations of positron emitting PARP-1 tracers to noninvasively measure the activation of DNA repair cascades invoked in tumors by external beam X-ray irradiation have been published using [ $^{18}\text{F}$ ]-FluorThanatrace and [ $^{18}\text{F}$ ]-Olaparib<sup>17,40</sup>. A direct comparison between the various PARP-1 imaging agents published to date is difficult, as various oncologic models and therapies have been utilized<sup>17,27,42–45</sup>. What distinguishes this work is the use of [ $^{18}\text{F}$ ]-PARPZ, with minimal degradation or metabolic products<sup>27</sup>, comparatively very high tumor localization (at roughly 10% Mean IA/g and 20% Maximum IA/g; Figs. 3, 4), sustained uptake (Fig. 5) and the use of potent alpha particle radiotherapy directed to a widely investigated prostate cancer radioligand target. While it is difficult to draw significant conclusions regarding the differences in PARP-1 expression

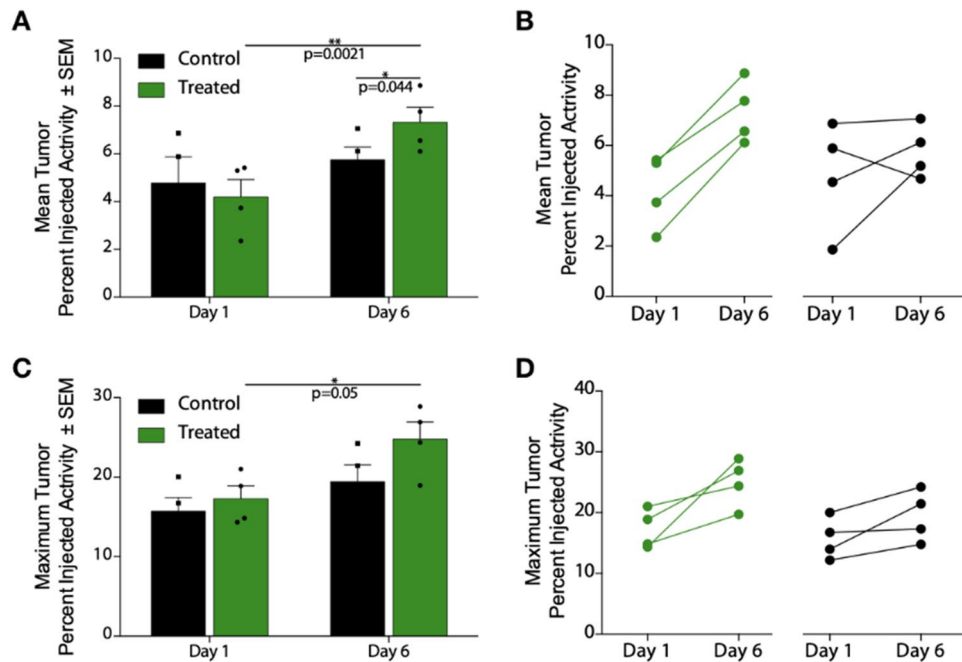


**Figure 4.**  $^{18}\text{F}$ -PARPZ Uptake and Response Data: Noninvasive PET imaging analysis was used to measure  $^{18}\text{F}$ -PARPZ uptake in treated and control groups. (A) Mean percent injected activity per gram (%IA/g) in the tumors did not significantly vary at the early imaging time point. After 6 days of  $^{225}\text{Ac}$ -PSMA-617 decay, the mean %IA/g significantly increased in the treated group ( $P < 0.05$ ). The two groups can be distinguished at this later time point by the mean uptake values ( $P < 0.005$ ). (B) Before-after plot of the individual changes in replicates' mean uptake values. (C) Maximum tumor voxel %IA/g is plotted, showing an increase for the treated animals between Day 1 and Day 3 ( $P < 0.05$ ). A trend for increased maximum  $^{18}\text{F}$ -PARPZ is present between the control and treated groups at Day 6, but is not significant. (D) Changes in individual replicates' maximum %IA/g.

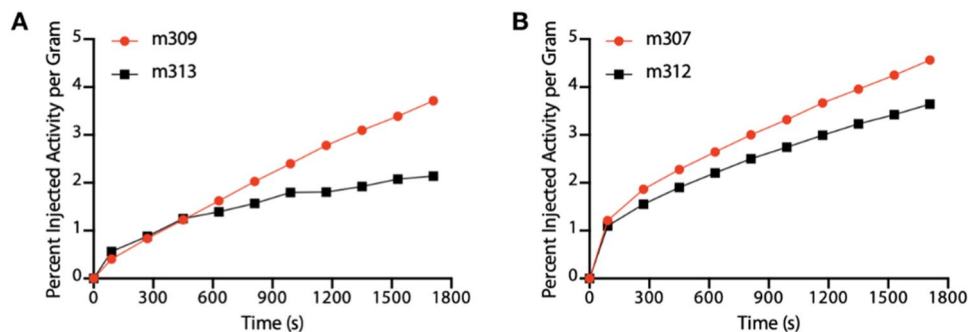


**Figure 5.** Rapid Uptake in  $^{225}\text{Ac}$ -PSMA-617 Treated Tumors: The tumor specific activity concentration of the PARP-1 tracer was determined in treated and control mice co-injected on camera. The results indicate a trend of more rapid uptake of  $^{18}\text{F}$ -PARPZ in tumors treated with alpha particle emitting  $^{225}\text{Ac}$ -PSMA-617 (red) over control saline treated subjects (black).

following treatment, we were able to generally correlated PARP-1 expression IHC with areas of radiotherapeutic localization by autoradiography (Fig. 6). PARP-1 is a druggable target in cancer for patients with BRCA deletions, including for prostate cancer patients. The combination of molecular radiotherapy with such agents is being widely investigated. A more thorough evaluation of specific DNA lesions induced by the radioligand therapy will be necessary to fully understand the utility of PARP PET imaging in the context of single agent and combination targeted radiotherapy.

The differences in tracer kinetics in the tumors between treated and control groups (Fig. 5) is an interesting observation. Our results demonstrate greater and more rapid localization of  $^{18}\text{F}$ -PARPZ in  $^{225}\text{Ac}$ -PSMA-617 treated tumors than those in the control group. In further planned studies, we intend to determine if the input characteristics of PARP-1 imaging tracer is indicative of treatment response. Limitations of this study include the evaluation of a high PARP-1 expressing prostate cancer cell model, and the use of immunohistochemistry

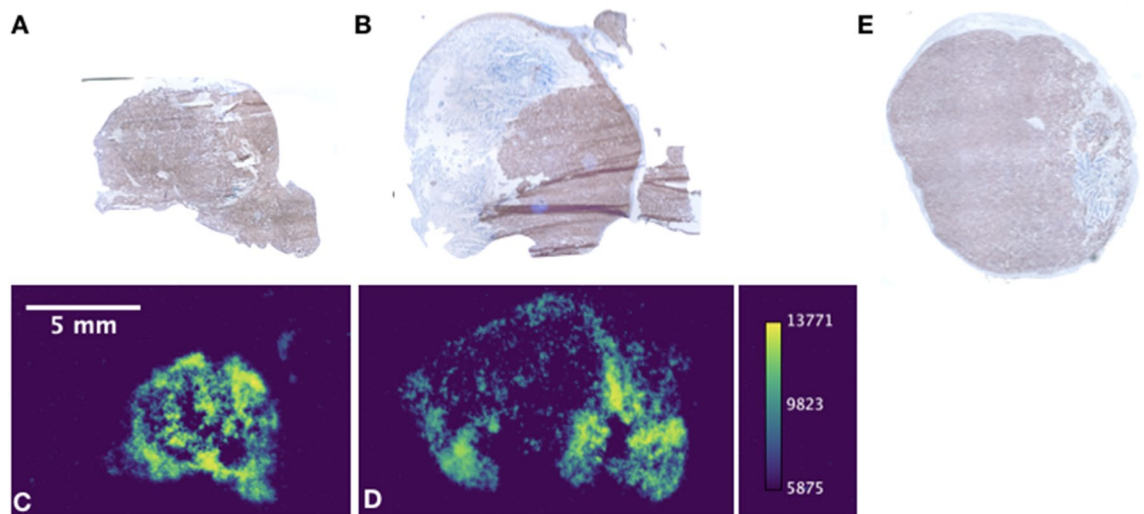


**Figure 6.** PARP-1 IHC and Autoradiography: Staining for PARP-1 was performed in tumors excised from treated and control animals. Autoradiographic images of tumor sections were acquired for [ $^{225}\text{Ac}$ ]-PSMA-617 in the treatment group. The areas of intense PARP-1 staining in treated tumors (A,C) and alpha particle emitting therapeutic (B,D) generally correlate. Staining of tumors in the control saline-treated group (E) tended to be less intense, but there was no significantly discernible difference in PARP-1 expression by IHC at this late sacrifice time point.

to evaluate changes in expression. A quantitative evaluation of the relative sensitivities of detection of PARP-1 expression changes across tumor cell lines by [ $^{18}\text{F}$ ]-PARPZ in vivo correlated by other molecular biotechniques is warranted to fully evaluate this promising new tool.

## Conclusions

We are able to measure significant increases in PARP imaging tracer localization to targeted  $\alpha$ -therapy treated tumors in a model system of prostate cancer. The improved imaging characteristics and stability of [ $^{18}\text{F}$ ]-PARPZ coupled with our institution's successful translation and implementation of a previous-generation agent, [ $^{18}\text{F}$ ] FTT, lay the ground-work for the initiation of clinical investigation of DNA damage response imaging in patients treated with both approved (Radium-223 dichloride) and investigational alpha particle radiotherapy.

## Data availability

The datasets generated and analyzed in the current study are available upon request to Dr. Thorek, thorekd@wustl.edu.

Received: 6 April 2022; Accepted: 26 July 2022

Published online: 29 July 2022

## References

- Jaffray, D. A. & Gospodarowicz, M. K. Radiation therapy for cancer. In *Cancer: Disease Control Priorities* 3rd edn, Vol. 3 (eds Gelband, H. *et al.*) (The International Bank for Reconstruction and Development/The World Bank, 2016).
- Abou, D. *et al.* Prostate cancer theranostics—An overview. *Front. Oncol.* **10**, 884 (2020).
- Humm, J. L. & Chin, L. M. A model of cell inactivation by alpha-particle internal emitters. *Radiat. Res.* **134**, 143–150 (1993).
- Kluetz, P. G. *et al.* Radium Ra 223 dichloride injection: U.S. Food and Drug Administration drug approval summary. *Clin. Cancer Res.* **20**, 9–14 (2014).
- Parker, C. *et al.* Alpha emitter radium-223 and survival in metastatic prostate cancer. *N. Engl. J. Med.* **369**, 213–223 (2013).
- Kratochwil, C. *et al.*  $^{225}\text{Ac}$ -PSMA-617 for PSMA-targeted  $\alpha$ -radiation therapy of metastatic castration-resistant prostate cancer. *J. Nucl. Med.* **57**, 1941–1944 (2016).
- Miederer, M. *et al.* Pharmacokinetics, dosimetry, and toxicity of the targetable atomic generator,  $^{225}\text{Ac}$ -HuM195, in nonhuman primates. *J. Nucl. Med.* **45**, 129–137 (2004).
- Meredith, R. F. *et al.* Safety and outcome measures of first-in-human intraperitoneal radioimmunotherapy with  $^{212}\text{Pb}$ -TCMC-trastuzumab. *Am. J. Clin. Oncol.* **41**, 716–721 (2018).
- Andersson, H. *et al.* Intraperitoneal alpha-particle radioimmunotherapy of ovarian cancer patients: Pharmacokinetics and dosimetry of ( $^{211}\text{At}$ -MX35 F(ab') $_2$ ) $_2$ —A phase I study. *J. Nucl. Med.* **50**, 1153–1160 (2009).
- McDevitt, M. R. *et al.* Feed-forward alpha particle radiotherapy ablates androgen receptor-addicted prostate cancer. *Nat. Commun.* **9**, 1629 (2018).
- Feuerrecker, B. *et al.* Activity and adverse events of actinium-225-PSMA-617 in advanced metastatic castration-resistant prostate cancer after failure of lutetium-177-PSMA. *Eur. Urol.* **79**, 343–350 (2021).
- McDevitt, M. R. *et al.* Tumor therapy with targeted atomic nanogenerators. *Science* **294**, 1537–1540 (2001).
- Rosenblat, T. L. *et al.* Treatment of patients with acute myeloid leukemia with the targeted alpha-particle nano-generator actinium-225-lintuzumab. *Clin. Cancer Res.* **28**, 2030–2037 (2022).
- Nikula, T. K. *et al.* Alpha-emitting bismuth cyclohexylbenzyl DTPA constructs of recombinant humanized anti-CD33 antibodies: Pharmacokinetics, bioactivity, toxicity and chemistry. *J. Nucl. Med.* **40**, 166–176 (1999).

15. Kratochwil, C. *et al.* Targeted  $\alpha$ -therapy of metastatic castration-resistant prostate cancer with 225Ac-PSMA-617: Swimmer-plot analysis suggests efficacy regarding duration of tumor control. *J. Nucl. Med.* **59**, 795–802 (2018).
16. Isaacsson Velho, P. *et al.* Efficacy of radium-223 in bone-metastatic castration-resistant prostate cancer with and without homologous repair gene defects. *Eur. Urol.* **76**, 170–176 (2018).
17. Wilson, T. C. *et al.* PET imaging of PARP expression using 18F-olaparib. *J. Nucl. Med.* **60**, 504–510 (2019).
18. Cornelissen, B. *et al.* Imaging DNA damage in vivo using gammaH2AX-targeted immunoconjugates. *Cancer Res.* **71**, 4539–4549 (2011).
19. Zhou, D. *et al.* Synthesis, [<sup>18</sup>F] radiolabeling, and evaluation of poly (ADP-ribose) polymerase-1 (PARP-1) inhibitors for in vivo imaging of PARP-1 using positron emission tomography. *Bioorg. Med. Chem.* **22**, 1700–1707 (2014).
20. Knight, J. C., Koustoulidou, S. & Cornelissen, B. Imaging the DNA damage response with PET and SPECT. *Eur. J. Nucl. Med. Mol. Imaging* **44**, 1065–1078 (2017).
21. Satoh, M. S. & Lindahl, T. Role of poly(ADP-ribose) formation in DNA repair. *Nature* **356**, 356–358 (1992).
22. Durkacz, B. W., Omidiji, O., Gray, D. A. & Shall, S. (ADP-ribose)<sub>n</sub> participates in DNA excision repair. *Nature* **283**, 593–596 (1980).
23. Shall, S. ADP-ribose in DNA repair: A new component of DNA excision repair. In *Advances in Radiation Biology* (ed. Lett, J. T.) 1–69 (Elsevier, 1984).
24. Ray Chaudhuri, A. & Nussenzweig, A. The multifaceted roles of PARP1 in DNA repair and chromatin remodelling. *Nat. Rev. Mol. Cell Biol.* **18**, 610–621 (2017).
25. Michel, L. S. *et al.* PET of poly (ADP-Ribose) polymerase activity in cancer: Preclinical assessment and first in-human studies. *Radiology* **282**, 453–463 (2017).
26. Makvandi, M. *et al.* A PET imaging agent for evaluating PARP-1 expression in ovarian cancer. *J. Clin. Invest.* **128**, 2116–2126 (2018).
27. Zhou, D. *et al.* Preliminary evaluation of a novel 18F-labeled PARP-1 ligand for PET imaging of PARP-1 expression in prostate cancer. *Nucl. Med. Biol.* **66**, 26–31 (2018).
28. Szabo, Z. *et al.* Initial evaluation of [(18F)DCFPyL for prostate-specific membrane antigen (PSMA)-targeted PET imaging of prostate cancer. *Mol. Imaging Biol.* **17**, 565–574 (2015).
29. Foss, C. A., Mease, R. C., Cho, S. Y., Kim, H. J. & Pomper, M. G. GCPII imaging and cancer. *Curr. Med. Chem.* **19**, 1346–1359 (2012).
30. Barretina, J. *et al.* The cancer cell line encyclopedia enables predictive modelling of anticancer drug sensitivity. *Nature* **483**, 603–607 (2012).
31. Cancer Cell Line Encyclopedia Consortium, and Genomics of Drug Sensitivity in Cancer Consortium. Pharmacogenomic agreement between two cancer cell line data sets. *Nature* **528**, 84–87 (2015).
32. Yardeni, T., Eckhaus, M., Morris, H. D., Huizing, M. & Hoogstraten-Miller, S. Retro-orbital injections in mice. *Lab Anim.* **40**, 155–160 (2011).
33. Jiang, W., Ulmert, D., Simons, B. W., Abou, D. S. & Thorek, D. L. J. The impact of age on radium-223 distribution and an evaluation of molecular imaging surrogates. *Nucl. Med. Biol.* **62–63**, 1–8 (2018).
34. Abou, D. S. *et al.* Whole-body and microenvironmental localization of radium-223 in naive and mouse models of prostate cancer metastasis. *J. Natl. Cancer Inst.* **108**, 380 (2016).
35. Nuñez, J. R., Anderton, C. R. & Renslow, R. S. Optimizing colormaps with consideration for color vision deficiency to enable accurate interpretation of scientific data. *PLoS ONE* **13**, e0199239 (2018).
36. Schindelin, J. *et al.* Fiji: An open-source platform for biological-image analysis. *Nat. Methods* **9**, 676–682 (2012).
37. Kossatz, S. *et al.* Direct imaging of drug distribution and target engagement of the PARP inhibitor rucaparib. *J. Nucl. Med.* **59**, 1316–1320 (2018).
38. Mateos-Pujante, A., Jiménez, M. C. & Andreu, I. Evaluation of phototoxicity induced by the anticancer drug rucaparib. *Sci. Rep.* **12**, 3434 (2022).
39. Kummar, S. *et al.* Advances in using PARP inhibitors to treat cancer. *BMC Med.* **10**, 25 (2012).
40. Sander Efron, S. *et al.* PARP-1 expression quantified by [18F]FluorThanatrace: A biomarker of response to PARP inhibition adjuvant to radiation therapy. *Cancer Biother. Radiopharm.* **32**, 9–15 (2017).
41. Thomas, A., Murai, J. & Pommier, Y. The evolving landscape of predictive biomarkers of response to PARP inhibitors. *J. Clin. Invest.* **128**, 1727–1730 (2018).
42. Zmuda, E., Malviya, G., Blair, A. & Boyd, M. Synthesis and evaluation of a radioiodinated tracer with specificity for poly (ADP-ribose) polymerase-1 (PARP-1) in vivo. *J. Med.* **58**, 8683–8693 (2015).
43. Huang, T., Hu, P., Banizs, A. B. & He, J. Initial evaluation of Cu-64 labeled PARPi-DOTA PET imaging in mice with mesothelioma. *Bioorg. Med. Chem. Lett.* **27**, 3472–3476 (2017).
44. Reiner, T., Keliher, E. J. & Earley, S. Synthesis and in vivo imaging of a 18F-labeled PARP1 inhibitor using a chemically orthogonal scavenger-assisted high-performance method. *Angew. Chem. Int. Ed. Engl.* **27**, 3472–3476 (2011).
45. Engelbach, J. A., Jannetti, S. A. & Carney, B. Discriminating radiation injury from recurrent tumor with [18 F] PARPi and amino acid PET in mouse models. *EJNMMI Res.* **8**, 1–10 (2018).

## Acknowledgements

This work was supported by R01-CA201035, and R01-CA229893. The Siteman Cancer Center is funded by NCI Cancer Center Support Grant #P30 CA091842.

## Author contributions

H.Z., P.L., A.M.H., D.A., A.V., N.B., D.Z., B.W.S., and D.L.J.T., performed the experiments. H.Z., D.A., P.L., A.V., N.B., W.J., D.U., B.W.S., F.D., D.Z., and D.L.J.T., analyzed the data. H.Z., D.A., S.C., B.E.R., N.F.T., M.R.M., B.B., F.D., D.Z., and D.L.J.T. devised the experiments and refined the study goals. D.Z., B.R., S.C., N.T., D.U., M.M., B.B., B.S. and D.L.J.T. prepared the figures. All authors evaluated and contributed to the writing of the manuscript.

## Competing interests

The authors declare no competing interests.

## Additional information

**Correspondence** and requests for materials should be addressed to D.Z. or D.L.J.T.

**Reprints and permissions information** is available at [www.nature.com/reprints](http://www.nature.com/reprints).

**Publisher's note** Springer Nature remains neutral with regard to jurisdictional claims in published maps and institutional affiliations.





**Open Access** This article is licensed under a Creative Commons Attribution 4.0 International License, which permits use, sharing, adaptation, distribution and reproduction in any medium or format, as long as you give appropriate credit to the original author(s) and the source, provide a link to the Creative Commons licence, and indicate if changes were made. The images or other third party material in this article are included in the article's Creative Commons licence, unless indicated otherwise in a credit line to the material. If material is not included in the article's Creative Commons licence and your intended use is not permitted by statutory regulation or exceeds the permitted use, you will need to obtain permission directly from the copyright holder. To view a copy of this licence, visit <http://creativecommons.org/licenses/by/4.0/>.

© The Author(s) 2022